Virtual Electrodes in Cardiac Tissue: A Common Mechanism for Anodal and Cathodal Stimulation

John P. Wikswo, Jr., Shien-Fong Lin, and Rashida A. Abbas
Living State Physics Group, Department of Physics and Astronomy, Vanderbilt University, Nashville, Tennessee 37235 USA

ABSTRACT Traditional cable analyses cannot explain complex patterns of excitation in cardiac tissue with unipolar, extracellular anodal, or cathodal stimuli. Epifluorescence imaging of the transmembrane potential during and after stimulation of both refractory and excitable tissue shows distinctive regions of simultaneous depolarization and hyperpolarization during stimulation that act as virtual cathodes and anodes. The results confirm bidomain model predictions that the onset (make) of a stimulus induces propagation from the virtual cathode, whereas stimulus termination (break) induces it from the virtual anode. In make stimulation, the virtual anode can delay activation of the underlying tissue, whereas in break stimulation this occurs under the virtual cathode. Thus make and break stimulations in cardiac tissue have a common mechanism that is the result of differences in the electrical anisotropy of the intracellular and extracellular spaces and provides clear proof of the validity of the bidomain model.

INTRODUCTION

Cardiac tissue can be stimulated electrically with the onset (make) or termination (break) of an electrical current that is applied with either a negative (cathodal) or positive (anodal) electrode (Dekker, 1970). However, classical, one-dimensional excitable cable theory cannot explain either anodal make or cathodal break stimulation in cardiac tissue. It has been assumed historically that cathodal make stimulation simply involves the direct depolarization of the cardiac cells immediately adjacent to the stimulating electrode and the subsequent opening of the activation, or m-gates of the transmembrane sodium channels. In the resting squid giant axon, a prolonged hyperpolarizing (anodal) stimulus opens the inactivation (or h-gates of the Na channels) such that when the anodal stimulus is terminated, the transmembrane potential V_m overshoots the resting value and produces anodal break excitation. However, this mechanism cannot explain anodal break excitation in cardiac muscle because there is little if any resting inactivation of the sodium channels (Beeler and Reuter, 1977; Ebihara and Johnson, 1980).

In this paper, we report a series of experiments in which we used epifluorescence imaging techniques to record directly the transmembrane potential distribution in the immediate vicinity of an electrode that injected current into the tissue. We present data that confirm unequivocally our earlier prediction using the cardiac bidomain model that point injection of either anodal or cathodal current into resting cardiac tissue produces simultaneously virtual cathodes and anodes that are the result of differences in the anisotropy of the electrical conductivity of the intracellular and extracellular spaces of the cardiac syncytium. We show that cathodal make stimulation is more complex spatially than expected from classical models of cardiac tissue, and that the primary distinction between cathodal make and anodal make excitations is which regions of tissue comprise the virtual anode and the virtual cathode. We also demonstrate that cathodal- and anodal break stimulations occur at the virtual anode. Because these experiments were conducted to verify specific theoretically predicted phenomena, we first review the cardiac bidomain model and the relevant predictions.

Received for publication 6 April 1995 and in final form 18 August 1995.

Address reprint requests to Dr. John P. Wikswo, Jr., Department of Physics and Astronomy, Vanderbilt University, Box 1807, Station B, Nashville, TN 37235. Tel.: 615-322-2977; Fax: 615-322-4977; E-mail: wikswojp@ctrvax.vanderbilt.edu.

0006-3495/95/12/2195/16 $2.00

THEORY

There have been extensive theoretical analyses in which the cardiac syncytium is modeled as two superimposed intracellular and extracellular domains, each with its own anisotropic electrical resistivity (Muler and Markin, 1977a,b,c; Tung, 1978; Geselowitz and Miller, 1983; Plonsey and Barr, 1984; Roth and Wikswo, 1986; Sepulveda and Wikswo, 1987). In these bidomain models, the distinct intracellular and extracellular conducting spaces are separated by cell membrane to form an anisotropic, three-dimensional cable or bidomain. Based upon experimental studies (Clerc, 1976), the electrical conductivities of the intracellular and extracellular spaces have differing anisotropies: $\sigma_{i\ell} = 0.17$ S/m, $\sigma_{it} = 0.019$ S/m; $\sigma_{e\ell} = 0.62$ S/m; and $\sigma_{et} = 0.24$ (i = intracellular, e = extracellular, ℓ = longitudinal, t = transverse). The anisotropy ratios for the two spaces ($\sigma_{i\ell}/\sigma_{it} = 8.9$ and $\sigma_{e\ell}/\sigma_{et} = 2.5$) differ, and it is just this difference that is responsible for the effects we report.

Equal anisotropy models

Despite the experimental evidence to the contrary, much of the early theoretical work with bidomain models assumed

for computational convenience that the anisotropy ratios for the intracellular and extracellular spaces were equal. These studies found minimal departures from monodomain models (Eisenberg et al., 1979; Henriquez and Plonsey, 1990a,b; Trayanova, 1994). As shown in Fig. 1 *A*, a model with equal anisotropy ratios for the electrical conductivities of the intracellular and extracellular spaces of the cardiac syncytium predicts that a strong cathodal make stimulus applied to the point electrode (*black dot*) would produce an oval-shaped region of tissue (*yellow to orange*), termed the virtual cathode, that is directly depolarized by the stimulating current. Activation would propagate outward from the edge of the virtual cathode, as shown by the curved yellow lines that correspond to the activation wave fronts separated by 2 ms. In this equal-anisotropy model, an anodal stimulus would produce a virtual anode of the same shape as the shaded ellipse, but the tissue inside the virtual anode would be hyperpolarized instead of depolarized, and there would be no propagating action potential.

Unequal anisotropy models

When the more realistic, differing anisotropy ratios are used for the intracellular and extracellular spaces, the model calculations are more difficult because it is necessary to solve a pair of coupled, nonlinear partial differential equations over the region modeled, rather than a single equation. Our two- and three-dimensional models predict a number of unexpected phenomena (Sepulveda et al., 1989; Roth and Wikswo, 1994; Wikswo, 1994a). From the perspective of cathodal and anodal make and break stimulation, the most important of these is that the point injection of cathodal current into cardiac muscle would produce a region of directly depolarized tissue (virtual cathode) as well as two regions of directly hyperpolarized tissue (virtual anodes) with complex geometrical shapes that are determined by the differences in the electrical anisotropies of the two domains. As we will show below, with cathodal or anodal make stimulation, action potentials propagate away from the virtual cathode and are delayed or possibly blocked by the

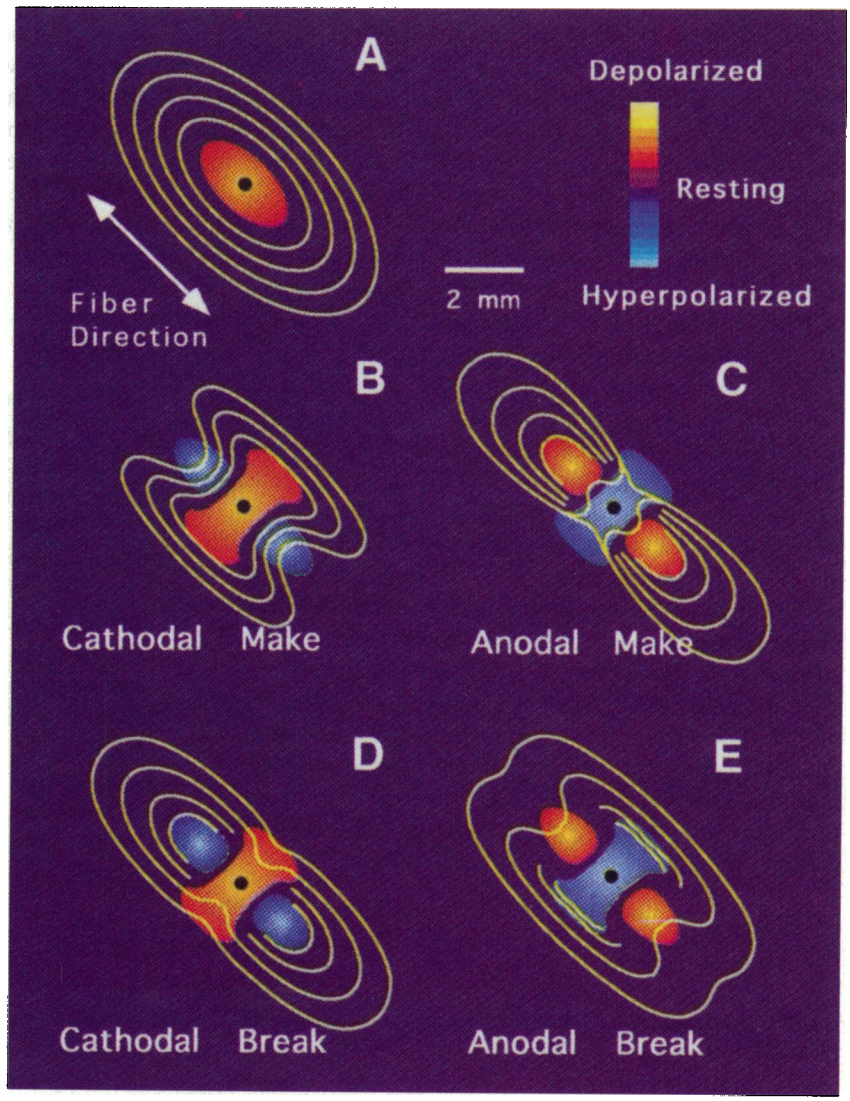

FIGURE 1 A schematic representation of the theoretical predictions of action potential propagation for point stimulation of cardiac tissue (based upon Sepulveda et al., 1989; Roth and Wikswo, 1994; Roth, 1995a). (*A*) Cathodal make stimulation in an equal-anisotropy model. An elliptical region of tissue would be directly depolarized (*orange*) by a strong point stimulus (*black dot*) and would act as a virtual cathode. An elliptical action potential wave front (*yellow lines separated by 2 ms*) would propagate away from the edge of the virtual cathode. (*B*) Cathodal make stimulation in a model with differing anisotropic conductivities for the intracellular and extracellular spaces. The virtual cathode is yellow to orange, and the virtual anode is blue. The resulting propagating wave front would initially have the transverse dog bone shape, but because of the greater longitudinal conduction velocity, the wave front would become elliptical by the time it was 5 mm from the stimulus electrode. (*C*) The same model as in (*B*), but for anodal make stimulation. A pair of action potential wave fronts propagating outward from the virtual cathodes (*orange*) merge and form an elliptical wave front within 1 cm of the stimulus electrode. (*D*) The same model for cathodal break stimulation. Early activation occurs from the virtual anodes (*blue*) along the fiber direction. (*E*) Anodal break stimulation, in which initial activation progresses transverse to the fibers from the dog-bone shaped virtual anode (*blue*).

virtual anode. These effects are not predicted by models with equal anisotropy ratios.

Cathodal make stimulation

For strong cathodal stimuli, as shown in Fig. 1 *B*, we predicted that the virtual cathode (*yellow to orange*) would be shaped like a dog bone aligned transverse to the fiber direction, with an adjacent pair of virtual anodes (*blue*) displaced from the stimulating electrode along the fiber axis (Sepulveda et al., 1989; Roth and Wikswo, 1994). The early activation wave front is also dog bone shaped, and propagation along the fiber direction is delayed so that the dog bone shape is maintained until the wave front has passed beyond the originally hyperpolarized, virtual anode regions. Measurements made at distances greater than 5 to 10 mm from the stimulus electrode would simply detect an elliptical activation wave front.

Anodal make stimulation

As shown in Fig. 1 *C*, model calculations have also predicted that with a strong, short anodal stimulus applied to resting tissue, the central dog bone shaped region beneath the stimulus electrode is now the virtual anode (*blue*), and more importantly, there would be a pair of adjacent virtual cathodes (*orange*) on either side of the virtual anode. If the stimulus is strong enough that the depolarization at the virtual cathodes reaches threshold levels, a wave front of activation is initiated in the longitudinal direction from the outer edge of each of the virtual cathodes. Propagation in the transverse direction is delayed until the hyperpolarization at the virtual anode has decayed. Eventually, the two wave fronts moving outward from the virtual cathodes merge to form an elliptical wave front that has a greater eccentricity than that produced by cathodal make stimulation. Because of the dependence of conduction velocity on both fiber direction and wave front curvature, this ellipse will become less eccentric as it propagates outward, so that by 1 cm from the stimulus, the cathodal make and anodal make wave fronts will be virtually indistinguishable. Hence activation begins at the edge of the virtual cathode for both cathodal and anodal make stimulation. Fig. 1, *B* and *C*, shows the novel prediction of unequal anisotropy models that anodal stimulation produces virtual cathodes.

Cathodal break stimulation

The bidomain model predicts that the virtual anode in Fig. 1 *D* provides the mechanism for cathodal break stimulation (Roth, 1995a). Cathodal break activation is generated with a long cathodal stimulus (S2) that is initiated during the refractory period of the action potential elicited by a preceding, short cathodal stimulus (S1), so that S2-make cannot activate the tissue. Cardiac tissue is inexcitable unless the sodium inactivation gates are open (Beeler and Reuter, 1977), which occurs at transmembrane potentials less than approximately −70 mV. Because the virtual cathode from S2 is strongly depolarized, the tissue within the virtual cathode is inexcitable; the virtual anode is, however, weakly hyperpolarized so that the sodium-inactivation gates are opened before the termination of the S2 stimulus. After the end of S2, large spatial gradients in V_m should cause diffusion of positive charge into the hyperpolarized virtual anode (Barach and Wikswo, 1992), which is transiently depolarized by this charge. Propagating activation is initiated at the virtual anode (*blue*) after a latency and does not propagate into the depolarized virtual cathode (*yellow to orange*), except at the ends furthest from the stimulus (Roth, 1995a).

Anodal break stimulation

A reversal of stimulus polarity exchanges the virtual cathode for a virtual anode and vice versa (Fig. 1 *E*), so that anodal break stimulation occurs by a mechanism similar to that for cathodal break stimulation. However, because the anodal dog bone is more strongly hyperpolarized than the adjacent virtual cathodes, the virtual cathodes contain insufficient charge to transiently depolarize the virtual anode, and the active membrane properties are necessary to explain anodal break stimulation. The membrane resistance (and therefore the RC time constant) is smaller for hyperpolarized membrane than for depolarized membrane because of inward rectifying K^+ channels (Roth, 1995a). The hyperpolarization therefore decays more rapidly, allowing the depolarization of the virtual cathode to diffuse into the hyperpolarized virtual anode sufficiently to transiently depolarize the tissue. Activation spreads initially in the transverse direction only because the inactivation gates of the tissue in the longitudinal direction are still closed because of depolarization at the virtual cathode. After a latency, a pair of short wave fronts move transversely out of the ends of the dog-bone-shaped virtual anode and subsequently grow quickly along the fiber direction. As before, the wave fronts would merge to form a closed wave front only after the activation has progressed beyond the virtual cathodes (*yellow to orange*) along the fiber axis (Roth, 1995a). Cathodal and anodal break stimulation do not occur in space-clamped tissue and hence are the result of the syncytial properties of the tissue and not the cell membrane alone. The complex patterns of virtual electrodes in the cardiac syncytium have not been visualized previously, nor have their varied roles in the initiation of activation from cathodal and anodal make and break stimulation been established experimentally.

MATERIALS AND METHODS

Imaging system

The imaging system consisted of a high-sensitivity cooled CCD camera with 12-bit resolution (Astromed Model 4100) and a 50-mm f1.8 objective

lens (Pentax), a 2-W argon laser with a 514-nm wavelength, a computer equipped with a frame-grabber board for acquiring digital images, and a separate computer that generated timing for the procedure. The duration of the CCD exposure was controlled by an acousto-optical beam deflector (NEOS N23080, Melbourne, FL) with an activation time in the microsecond range. Pixel images (100 × 100) covering a 7.5 mm × 7.5 mm field of view were taken with a 0.5-ms CCD exposure. The depth of focus of the imaging setup was approximately 2 mm.

Heart preparation

White New Zealand rabbits weighing 2 to 3 kg were preanesthetized with intramuscular ketamine (50 mg/kg). Intravenous sodium pentobarbital (50 mg/kg) containing 2000 units of heparin was given for anesthesia. The hearts were removed quickly, mounted on a Langendorff apparatus, and perfused with Tyrode's solution containing 130 mM NaCl, 4 mM KCl, 11 mM dextrose, 1.8 mM $CaCl_2$, 0.6 mM $MgCl_2$, 24 mM $NaHCO_3$, and 1.2 mM NaH_2PO_4 at pH 7.4. The Tyrode's solution was maintained at 37°C and was saturated with a 95% O_2/5% CO_2 gas mixture. All experiments were conducted in accordance with National Institutes of Health regulations for the ethical use of animals in research and were approved in advance by the Vanderbilt Institutional Animal Care and Use Committee.

The experiments were performed on the left ventricle of Langendorff-perfused isolated rabbit hearts. The voltage-sensitive dye di-4-ANEPPS (Molecular Probes, Eugene, OR) was added to the Tyrode's solution, which perfused the heart at a concentration of 0.5 μM. The dye molecules bind to the cell membrane and, when excited by blue-green light, emit red fluorescence with an intensity proportional to the transmembrane potential (Cohen and Lesher, 1986). Diacetylmonoxime (15 mM) (Sigma) was added to the Tyrode's solution to block muscle contraction. The isolated heart was pushed gently with a plastic supporting plate against another plastic plate with a circular opening to provide a reflection-free window for imaging the heart. A pair of platinum wires mounted along the edge of the window were used for S1 stimulation to provide refractory tissue for the S2 stimulation. The S2 stimuli were delivered through a teflon-insulated, 100-μm platinum wire wound two and a half turns around a supporting suture that was stretched across the window. The teflon insulation was removed from a central kink in the wire to allow the platinum to contact the epicardium over an area of 100 μm by 200 μm. A 1-cm-diameter spiral of silver wire situated at the center of the supporting plastic plate on the opposite side of the heart was used as the reference electrode for S2 stimulation.

Stimulation and image acquisition

Refractory tissue

The heart was paced at a constant rate (typically 120–180 beats/min) with a train of pacing (S1) stimuli applied to the electrodes at the edge of the field. After the heart reached steady-state response, a baseline, resting image was acquired at a time $t = t_r$ just before an S1 stimulus. Five more S1 stimuli were applied. An S2 stimulus was delivered to the refractory tissue by the central electrode 78 ms after the last S1. The second, refractory image was acquired during the first 2 ms of S2. This process was repeated until we had acquired eight image pairs. To correct for spatial variations in tissue illumination and fluorescence, the images recorded after a stimulus were divided by the preceding baseline image. As described in detail below, the images were also corrected for fluctuations in laser intensity. The eight corrected images were then averaged. The resulting transmembrane potential images were digitally filtered with a Wiener adaptive spatial filter to enhance the signal-to-noise ratio (Lim, 1990). To prevent the filter from spreading the 1-to-4 pixel-wide image of the stimulus wire that spanned the middle of the image, those pixels were removed digitally and replaced with normally distributed random numbers with a mean and a variance equal to those of the neighboring pixels so that they would not affect the adjacent pixels during subsequent filtering. A faint indication of the vertical wire can be seen in several of the images presented in the Results.

Make excitation

Similar methods were used to image activation after make excitation of resting cardiac tissue, except that S1 was delivered from the central electrode and the tissue response to S1 was recorded. Because of the limitations of the camera frame rate, we used boxcar averaging techniques to acquire a series of sequential, synchronized images that were effectively separated by 2 ms. The heart was paced at a constant rate (typically 120 to 180 beats/min) from the central electrode with a train of 1-ms pacing (S1) stimuli. After steady state was reached, a baseline image was acquired just before an S1 stimulus, the second image (0 ms) during the next S1 stimulus, the third image (2 ms) 2 ms after the third S1, and so on. Eight images at each of six sequential times were recorded over a total of 48 stimuli. For each time, the eight images were averaged and divided by the baseline image. All images were spatially filtered as described above. For anodal S1 stimuli, bipolar recording electrodes at the edge of the window were used to confirm that anodal stimulation occurred at the central electrode and did not propagate into the tissue from the distant, cathodal electrode.

Break excitation

Boxcar averaging techniques similar to those used for make excitation were used for break excitation, but with a different stimulation protocol. After steady state was reached, the heart was paced with a train of six 4-ms S1 stimuli followed by a single 150-ms to 180-ms S2 stimulus. The baseline image was acquired just before the last S1. There would then be six more S1 stimuli; the second image was recorded at the end (break) of the second S2; there would be six more S1 stimuli; the third image was acquired 3 ms after the second S2, and so on. The process was repeated until four images at each of eight sequential times had been acquired over a total of 224 stimuli. The image processing was as described above. To ensure that the S2 stimulus onset occurred during the refractory (unexcitable) period from the preceding S1 stimulus, S1-S2 intervals of 100 ms and 80 ms were used for cathodal break and anodal break stimulation, respectively, and a long (180 ms and 150 ms) S2 duration allowed the cathodal break and anodal break to occur when the tissue was fully excitable.

The need for strong stimuli

Weak cathodal stimuli will produce propagated activity from a small virtual cathode, with a size at threshold given by the liminal length. As predicted by the model, the dog-bone-shaped virtual cathode is present only for strong cathodal stimuli. Anodal make and both cathodal and anodal break stimulation require strong virtual cathodes and anodes and hence high stimulus strengths. Break excitation requires that these stimuli be applied for longer than 150 ms. However, repeated application of long stimuli many times the threshold intensity can result in tissue damage under the electrode. We found that, for the cathodal and anodal make experiments, a stimulation current of 10 mA was a good compromise between large virtual cathodes and anodes and minimal tissue damage. For the break experiments, bubble formation under the electrode was a direct result of electrolysis due to the long duration of stimulation currents and suggests the possibility of underlying tissue damage. The advantage of our imaging approach, in contrast to earlier experiments using fixed electrode arrays with off-line data analysis, is that cumulative tissue damage from repeated stimulation could be identified immediately from the images of the membrane potential distribution as areas having a stationary level of fluorescence and hence not supporting an action potential. The resulting images in which tissue damage could be identified were discarded, and the heart was repositioned to study an undamaged region of tissue.

Image rotation and normalization

Each of the four different modes of excitation was observed in multiple experiments. Although the shapes of the virtual electrodes and the subsequent activation patterns were qualitatively consistent between experiments, there was some variability in the shape of the patterns both between recording sites on an individual heart and between hearts. The fiber direction and hence the virtual electrode orientation relative to the camera were different at each recording site. In addition, the tissue fluorescence corresponding to maximum depolarization varied between recording sites and animals. In our previous study of the virtual cathode (Wikswo et al., 1991), we used measurements of the virtual cathode at selected angles to construct the average virtual cathode pattern and thereby average over inter-experiment variation. In the present work, we have expanded upon this approach to construct automatically a composite set of images representing the average sequence of activation for each mode of stimulation by averaging the results of the appropriate experiments.

The first step was to align the images for each set of experiments. To do this, we determined the x-y coordinates of the center of the central dog bone in the first frame of a sequence by computing the center of intensity of the dog bone, which is the mean of the intensity squared weighted by the x or y coordinate. To rotate the images to a common orientation, we determined the longest axis of symmetry of the dog bone, corresponding to the direction transverse to the fibers, by first dividing the dog bone into right and left halves as defined by a vertical axis through the center of intensity. The coordinates of the center of intensity of each of these halves were determined as before, and a least-squares fit through these two points and the center of the dog bone determined the dog bone axis. We then computed the angle between the dog bone axis and the horizontal axis of the image. All images in a sequence were then rotated by this same angle so that the dog bone axis in the first frame was vertical. Thus the direction of fast propagation, i.e., the fiber direction, is horizontal in all frames of the sequence. After rotating, the images were cropped to a 71 × 71 pixel region centered about the center of intensity, so that all images would have the same number of pixels regardless of the original orientation of the pattern.

Because of inter-site and inter-animal differences in dye absorption and fluorescence intensity, the averaging of images required that each image be normalized beforehand, so that a pixel value of zero corresponds to resting tissue and a value of 1 corresponds to maximum depolarization. The fluorescence intensity $F(x,y,t)$ as measured in a single exposure of the camera is determined by the transmembrane potential of the tissue $V(x,y,t)$, the spatially varying efficiency of fluorescence of the tissue $E(x,y)$, and the time-dependent laser intensity $L(t)$. Ideally, $E(x,y)$ would be the same at all values of x and y for homogeneously stained tissue, and $L(t)$ would be a constant for a perfectly stable laser and a totally repeatable acousto-optic modulator; in our analysis, we account for non-ideal behavior of $E(x,y)$ and $L(t)$, i.e.,

$$F(x, y, t) = L(t)E(x, y)V(x, y, t). \quad (1)$$

As stated above, we recorded a reference image $F_r(x,y,t_r)$ of resting tissue at $t = t_r$, so that

$$F_r(x, y, t_r) = L(t_r)E(x, y)V_r(x, y, t_r). \quad (2)$$

To eliminate the effects of spatial variations in fluorescence due to tissue inhomogeneities, i.e., $E(x,y)$, the intensity of each pixel of the image at time t is divided by the intensity of the corresponding pixel of a reference image of the same region at rest at $t = t_r$,

$$F(x, y, t)/F_r(x, y, t_r) = \{L(t)/L(t_r)\}\{V(x, y, t)/V_r(x, y, t_r)\}. \quad (3)$$

We corrected for the laser fluctuations $L(t)$ by identifying a 20 × 20 cluster of $N = 400$ calibration pixels in each sequence of images for which the tissue did not depolarize within the time interval examined. Typically, these pixels were located in one corner of the rotated images. The mean intensity of the resting calibration pixels at points x_c,y_c in the frame at time t is given by

$$F_c(t) = 1/N \Sigma\{L(t)E(x_c, y_c, t)V_r(x_c, y_c, t)\}. \quad (4)$$

If we assume that the tissue in the calibration pixels remains at rest throughout the sequence, then $V_r(x_c,y_c,t_r) = V_r(x_c,y_c,t)$, and it follows that the effect of laser fluctuations can be eliminated by dividing each image by the corresponding mean intensity of the calibration pixels

$$\{F(x, y, t)/F_c(t)\}/\{F_r(x, y, t_r)/F_c(t_r)\} = V(x, y, t)/V_r(x, y, t_r). \quad (5)$$

The commonly stated measure of fluorescence is the fractional change in fluorescence $\Delta F/F$,

$$\Delta F/F = \{F(x, y, t) - F_r(x, y, t_r)\}/F_r(x, y, t_r) = F(x, y, t)/F_r(x, y, t_r) - 1. \quad (6)$$

When corrected for fluctuations in laser efficiency, the observed $\Delta F/F$ equals $\Delta V/V$, or

$$\Delta V(x, y, t)/V(x, y, t_r) = \{F(x, y, t)/F_c(t)\}/\{F_r(x, y, t_r)/F_c(t_r)\} - 1. \quad (7)$$

All that remains is to identify a constant K multiplying Eq. 7 for a particular sequence such that all images in every sequence would span the same range of intensity between resting and depolarized tissue, i.e., from 0 to 1. To do this, we identify a cluster of pixels in an image at time t_d that were maximally depolarized by a propagating wave front (in contrast to those depolarized directly by the stimulus pulse). It can be shown that for these depolarized pixels

$$1/K = \{F(x_d, y_d, t_d)/F_c(t_d)\}/\{F_r(x_d, y_d, t_r)/F_c(t_r)\} - 1. \quad (8)$$

The normalized image intensity $I(x,y,t)$ that we averaged across experiments is thus

$$I(x, y, t) = K[\{F(x, y, t)/F_c(t)\}/\{F_r(x, y, t_r)/F_c(t_r)\} - 1].$$

The images that corresponded to the standard deviation of the average value of each pixel were also computed to determine the effects of inter-site and inter-animal variation on each average image. For the quantitative analysis of the virtual electrode shapes with the different stimuli, the images from the second through fourth quadrants of the rotated and normalized $t = 0$ image for each experiment were reflected across the x and y axes before computation of the averages so that all data could be combined into a single image in the first quadrant, as was done in our previous analysis (Wikswo et al., 1991).

RESULTS

Refractory tissue

Fig. 2 shows images of the transmembrane potential distribution for injection of cathodal and anodal current into the depolarized, unexcitable epicardium of an isolated perfused rabbit heart. The data are consistent with both the numerical models (Sepulveda et al., 1989; Roth and Wikswo, 1994; Wikswo, 1994a; Roth, 1995a) and observations by others (Knisley et al., 1994; Neunlist and

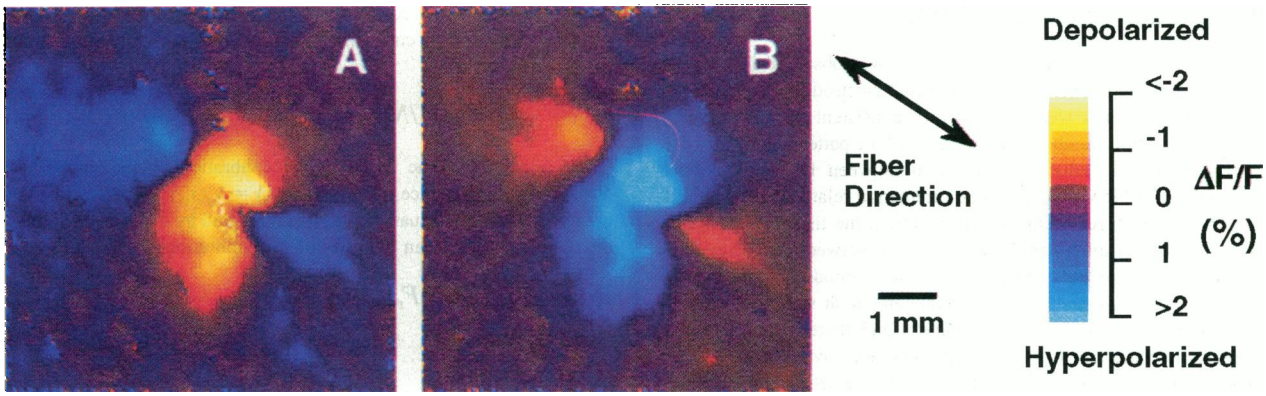

FIGURE 2 False-color images of the transmembrane potential associated with injection of current into refractory cardiac tissue. (*A*) The image for a −10 mA, 2-ms cathodal S2 stimulus applied at a point electrode. Note the dog-bone shaped virtual cathode (*orange*) and the pair of adjacent virtual anodes (*blue*). The fiber orientation is from lower right to upper left. The color bar shows the fractional change in fluorescence. (*B*) The complementary image for a +10 mA, 2-ms anodal S2 stimulus at the same location on the heart. Note that the dog bone is now the virtual anode (*blue*), whereas the adjacent areas are virtual cathodes (*orange*).

Tung, 1994a,b, 1995; Knisley and Davis, 1994; Knisley, 1995), and validate our measurement technique.

Images from typical experiments

Our measurement techniques can also be applied to visualizing the propagation of activation after make excitation of resting, excitable tissue. Fig. 3, *A* and *B*, shows the initial activation patterns for anodal and cathodal point stimulation, as well as the subsequent outwardly propagating wave fronts with a frame interval of 2 ms. To show the changes in transmembrane potential associated with propagation, i.e., the additional tissue depolarized since the preceding frame and hence the shape and width of the propagating depolarization wave front, each averaged image was subtracted from the following one. The post-stimulus images shown for times greater than 0 ms are these difference images. Cathodal stimulation (1 ms, −10 mA) in Fig. 3 *A* shows a clear dog bone virtual cathode and adjacent virtual anodes. By 2 ms, activation has spread outward from the virtual cathode to tissue within 2 mm of the stimulus site. The images at 4 and 6 ms show a central filament of delayed activation along the fiber axis that overlies the region of the earlier virtual anodes. The activation spreads past the virtual anode region only by 8 ms, so that the filament disappears.

Fig. 3 *B* shows the complementary hyperpolarized, dog-bone-shaped virtual anode transverse to the fiber direction, and a pair of adjacent, depolarized virtual cathodes along the fibers that were elicited by a 1 ms +10 mA anodal make stimulus. These two virtual cathodes serve as the sites of origin of an outwardly propagating action potential wave front. At 2 ms, activation is expanding in all directions from the pair of virtual cathodes, so that the activation along the fiber direction is 50% further than for the cathodal make stimulus of the same duration and strength in Fig. 3 *A*, while it has progressed only half as far in the transverse direction. The filament of delayed activation is again present for the 4 and 6 ms images, but is transverse to the fiber direction; it has disappeared by 8 ms, when the activation has propagated in the transverse direction beyond the area covered by the dog-bone-shaped virtual anode. Because the propagating wave front at 8 ms originated from the pair of virtual cathodes along the fiber direction, the anodal make wave front has a greater eccentricity than that produced by cathodal make, as shown by the theoretical predictions (Roth, 1995a) in Fig. 1, *B* and *C*.

Fig. 3 *C* shows the result of cathodal break stimulation. In the 0 ms frame immediately after the end of the 180-ms, −2 mA cathodal stimulus, the transverse dog bone virtual cathode is depolarized, while the longitudinal virtual anode is hyperpolarized. The circular, multicolored region at the center of each frame is from bubbles at the electrode. The virtual anodes and cathode are not apparent in the 3 ms frame, and activation first appears in the 6 ms frame as a pair of wave fronts propagating along the fiber direction, originating after a one-frame latency from the site of the virtual anode.

Fig. 3 *D* shows the results of anodal break stimulation. In the 0 ms frame immediately after the end of the 150-ms, +3 mA anodal stimulus, the transverse dog bone virtual anode is hyperpolarized, whereas the longitudinal virtual cathodes are depolarized. Activation first appears in the 6 ms frame as a pair of short wave fronts propagating transverse to the fiber direction, originating after a one-frame latency from the site of the virtual anode. These wave fronts move slowly away from the electrode while extending quickly along the fiber direction, eventually merging in the last frame to form a closed, nearly elliptical wave front. A subsequent frame (not shown) has a delayed longitudinal filament of activation due to the effects of the early, longitudinal virtual cathodes.

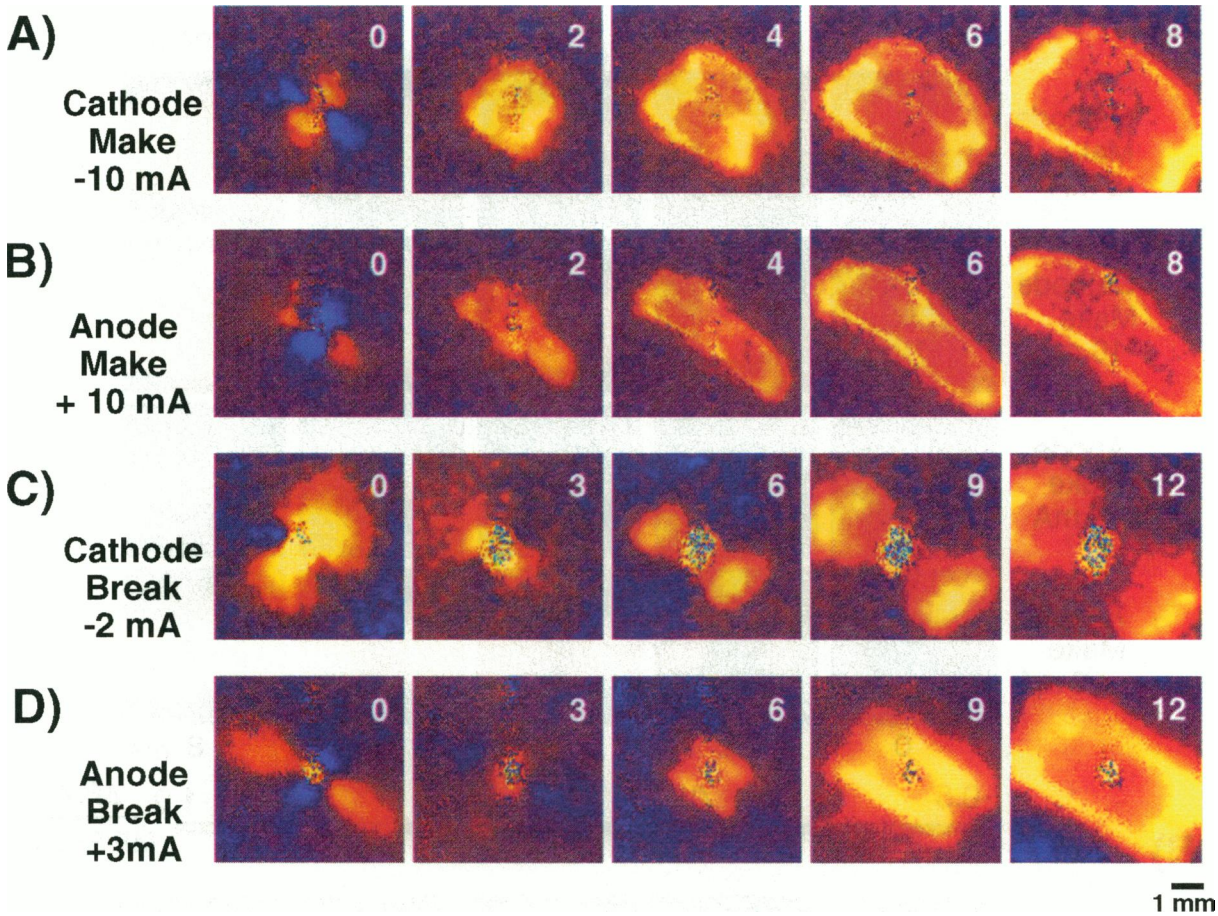

FIGURE 3 False-color images of the transmembrane potential associated with injection of current into fully repolarized, excitable cardiac tissue. The number inside each frame is the time in milliseconds. Upper two rows: make stimulation. (*A*) Cathodal make stimulation with a 1-ms, −10 mA S1 stimulus current; (*B*) 1-ms, +10 mA S1 anodal make stimulation of the same heart. Lower two rows: break stimulation. (*C*) 180-ms, −2 mA cathodal break S2 stimulation of another heart; (*D*) 150-ms, +3 mA anodal break S2 stimulation of a third heart. For each row, the leftmost images are at the end of the S2 stimulus (0 ms), and the other images were at 2-ms (*A* and *B*) or 3-ms (*C* or *D*) intervals thereafter. The direction of the epicardial fibers from lower right to upper left is evidenced by the shape of the virtual electrode pattern and the elongation of the propagating wave front in the last two images of each sequence. The color scale is the same as in Fig. 2.

Averaged propagation images from multiple experiments

We conducted multiple experiments at a total of ten locations on seven rabbit hearts, so that we obtained images suitable for averaging from eight cathodal make, eight anodal make, four cathodal break, and two anodal break experiments, at a variety of stimulus strengths. (Make-excitation stimulation experiments from multiple sites on 8 additional rabbit hearts and break-excitation experiments on 4 hearts were conducted with different experimental parameters that were not consistent with the images used to compute these averages, or were eliminated because of the possibility of tissue damage. The results of these experiments, while consistent with the results we present, are not included in this analysis). All of the data showed excellent, qualitative agreement. The most obvious differences observed were in the exact shapes of the virtual anodes and cathodes and the wave fronts that propagated from them, as would be expected, for example, from inter-animal variations in how coronary vasculature affected the images. In all cases, the results were fully consistent with the theoretical predictions. We used the image-processing techniques outlined in the previous section to compute the average and standard deviation images for each type of stimulation for those experiments that used the same stimulus strength. Fig. 4 shows the average and standard deviation images resulting from cathodal and anodal make stimulation at ±5 and ±10 mA. The actual images rather than the difference images are shown. The results are consistent with those in Fig. 3, except that the later wave fronts are more spread out because of inter-site and inter-animal variations in conduction velocity and excitability.

Cathodal make

The dog-bone-shaped virtual cathode is clearly evident in the leftmost (t = 0) cathodal make frames in the top two rows of Fig. 4 *A*, with the dog bone shape and the adjacent

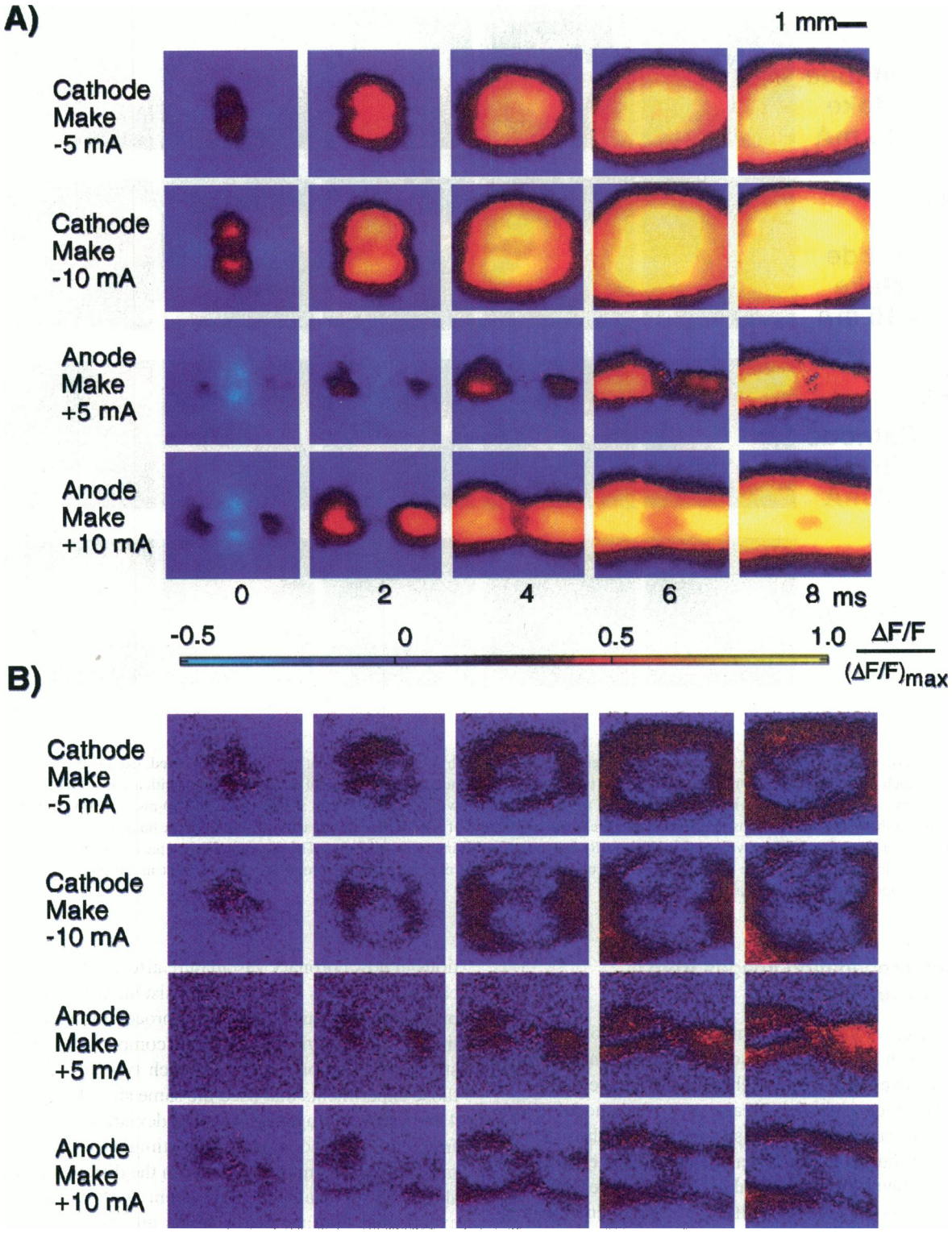

FIGURE 4 (*A*) False-color images of the average transmembrane potential associated with injection of current into excitable cardiac tissue. Each sequence represents the average of four separate experiments. The top two rows show cathodal make stimulation with a 1-ms stimulus current of −5 and −10 mA. The bottom two rows show anodal make stimulation with a 1-ms stimulus current of +5 and +10 mA. The time in milliseconds is labeled below the images with the $t = 0$ image acquired during injection of the stimulus current. Fiber axis is in the horizontal direction. The fractional change in fluorescence, $\Delta F/F$, as a fraction of the maximum change (which corresponds to fully depolarized tissue), is shown in the color bar. (*B*) False-color images showing the standard deviation from the mean for each of the average images. The color scale and fiber orientation are the same as in (*A*).

hyperpolarized virtual anodes along the fiber (horizontal) axis being more prominent in the −10 mA image. The 8 ms activation patterns are less elliptical for −10 mA stimulation than for −5 mA, consistent with the larger dog bone and stronger on-axis hyperpolarization. The web of delayed activation is readily apparent in the 2 ms and 4 ms frames. Because the dog bone virtual cathode is larger at −10 mA than at −5 mA, more tissue is depolarized at 8 ms in the transverse direction for the −10 mA stimulus; depolarization along the fiber axis is restricted by the pair of virtual anodes and hence does not extend with increased I_s. The standard deviation images in the top two rows of Fig. 4 *B* show that the virtual electrodes are quite consistent for all of the measurements, but differences in conduction velocity cause the standard deviation to increase with time in the vicinity of the edge of the depolarization wave front.

Anodal make

The lower two rows of Fig. 4 *A* show that anodal make excitation occurs at the virtual cathodes adjacent to the dog-bone-shaped virtual anode. As was the case for cathodal make excitation, the virtual electrodes are larger, stronger, and more clearly defined for the +10 mA stimulation, and by 8 ms a larger area of tissue is activated for the stronger stimulus, both longitudinally and, on either side of the vertical axis defined by the virtual anode, transversely. The standard deviation images in the lower two rows of Fig. 4 *B* confirm that the virtual electrode patterns are consistent between animals and that the variation in conduction velocity leads to blurring of the depolarization wave front. The right-left asymmetry of the later +5 mA, anodal make images in Fig. 4 *A* is consistent with larger standard deviations in the corresponding images of Fig. 4 *B*, apparently because of an asymmetric tissue response in one of the experiments.

Cathodal break

The top row of Fig. 5 *A* shows the averaged data for −2 mA, 180-ms cathodal break stimulation. The most strongly

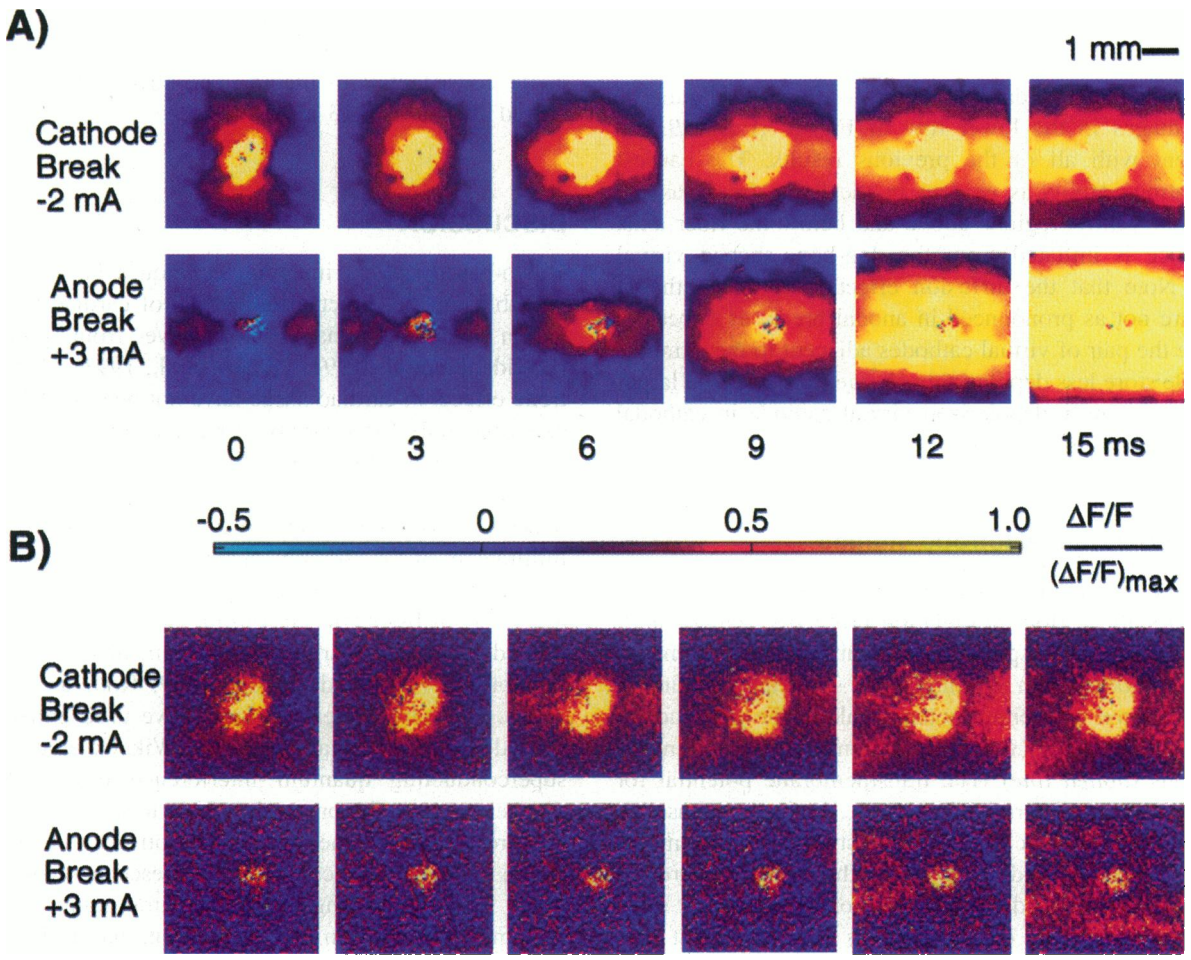

FIGURE 5 (*A*) False-color images of the average transmembrane potential associated with break stimulation of cardiac tissue. The top row shows cathodal break stimulation with a 180 ms, −2 mA S2 pulse and represents the average of four separate experiments. The bottom row shows anodal break stimulation with a 150-ms, +3 mA S2 pulse and represents the average of two experiments. The time in milliseconds is labeled below the images, with the $t = 0$ image acquired just before the offset of the S2 stimulation pulse. (*B*) False-color images showing the standard deviation for the average images. The color scale and fiber orientation are the same as in Fig. 4.

depolarized tissue, in the form of the yellow circular region, remains essentially static in all frames and is the lingering result of the prolonged depolarization of the tissue by the long stimulus pulse. The dog bone virtual cathode is easily seen in the $t = 0$ frame. By the 3 ms frame, the furthest edges of the virtual cathode have diffused to the extent that the outer edges of the depolarized region (red) are now circular. In the next frame (6 ms), excitation of the tissue underneath the two virtual anodes has begun, in that the depolarization on the axis away from the stimulus site is increasing, and depolarization (*yellow*) is appearing in these regions by the 9 ms frame. Outward propagation in the form of an expanding red envelope is occurring in the last frame. In the standard deviation images in the top row of Fig. 5 *B*, the central region shows that there is, as expected, significant variation in the response in the tissue in the immediate vicinity of the stimulus electrode due to bubbles at the electrode visible in Figs. 3 *C* and 5 *A*. The standard deviation outside this region increases in time as the propagation progresses in the later frames, consistent with the experimental variation in conduction velocity.

Anodal break

The average and standard deviation for the +3 mA anodal break images in the lower row of Fig. 5, *A* and *B*, are consistent with all of the previous results. The earliest propagating activity is evident in the 9 ms frame as the horizontal yellow regions above and below the fiber axis, and hence is initiated from the dog-bone-shaped virtual anode. Note that the diffusion effects seen for cathodal break are not as pronounced in anodal break, as expected, because the pair of virtual cathodes adjacent to the stimulus electrode store less depolarizing charge than does the larger and more strongly depolarized virtual cathode in cathodal break stimulation.

Averaged virtual electrode images

Fig. 6 shows the single-quadrant virtual electrode ($t = 0$) images for the various stimulation protocols (*leftmost column*) and the corresponding standard deviation images (*rightmost column*). In the middle, we show the variation in the normalized membrane potential along the longitudinal and transverse axes (*solid lines*) along with the standard deviations (*dotted line*). The transmembrane potential for resting tissue, as determined at $t = t_r$, is the zero baseline (*dashed line*). It is clear that the stronger the stimulus current, the larger and stronger are the virtual electrodes. The largest standard deviations are for anodal break excitation, for which the central bubbles were the most pronounced, and for which we had the least data. In the cathodal and anodal make data, the standard deviations are largest midway between the stimulus electrode and the edge of the image, reflecting variation in the exact size of the virtual electrodes between experiments. The second column shows that along the fiber axis, cathodal make stimulation produces depolarization close to the electrode, but hyperpolarization of up to 40% of the action potential amplitude from 0.8 mm to 2.2 mm from the electrode. The stronger the stimulus, the stronger the hyperpolarization. Identical effects are seen in anodal make stimulation, but of the opposite sign. The tissue response is largest in the vicinity of the stimulating electrode and has the largest response of the opposite sign at an average distance of 1.43 ± 0.06 mm. On the fiber axis, the virtual cathodes and anodes are clearly demarcated as the transmembrane potential crosses zero, at 0.97 ± 0.08 mm. As expected from theory (Sepulveda et al., 1989; Roth and Wikswo, 1994), the location of the zero crossing is the same for both cathodal and anodal make stimulation and does not depend upon stimulus strength. The hyperpolarization is not as pronounced in the cathodal break data as in the make data, possibly because of changes in the membrane conductance, i.e., nonlinearities, associated with the depolarization. The zero crossing for the average cathodal break data occurs at 1.65 mm, whereas that for anodal break occurs at 0.86 mm. The data in the third column demonstrate that transverse to the fiber axis, the tissue is depolarized everywhere for cathodal stimulation and hyperpolarized everywhere for anodal stimulation, again consistent with theory. The strongest response occurred at 0.62 ± 0.13 mm.

DISCUSSION

Video-based optical imaging techniques have proved invaluable for the direct visualization of cardiac tissue activation and the dynamics of wave front propagation (Davidenko et al., 1991; Pertsov et al., 1993). Virtual electrode effects in cardiac tissue have not been widely studied experimentally for a variety of reasons: the potential distributions associated with the virtual electrodes are often dismissed as "stimulus artifact"; the small spatial extent of these patterns requires dense electrode arrays within several millimeters of the stimulus electrode; and the extracellular isopotentials are approximately ellipsoidal for both equal and unequal bidomain anisotropies, so that the dog-bone-shaped patterns appear only in the transmembrane potential distribution (Sepulveda et al., 1989; Roth and Wikswo, 1994). Our earlier measurements have used either closely spaced arrays of bipolar electrodes (Wikswo et al., 1991) or superconducting quantum interference device (SQUID) magnetometers (Staton et al., 1993) to confirm several of the predictions of the unequal-anisotropy model. In this study, we extend the cardiac epifluorescence imaging technique by incorporating a wide dynamic-range acquisition system, short-duration laser excitation, and an incremental timing sequence to study in detail the initiation and propagation of activation in the immediate vicinity of a point stimulating electrode. Our technique provides significantly higher spatial resolution (75 μm) than does the scanning laser system (1 mm) used by Knisley (1995). The fact that

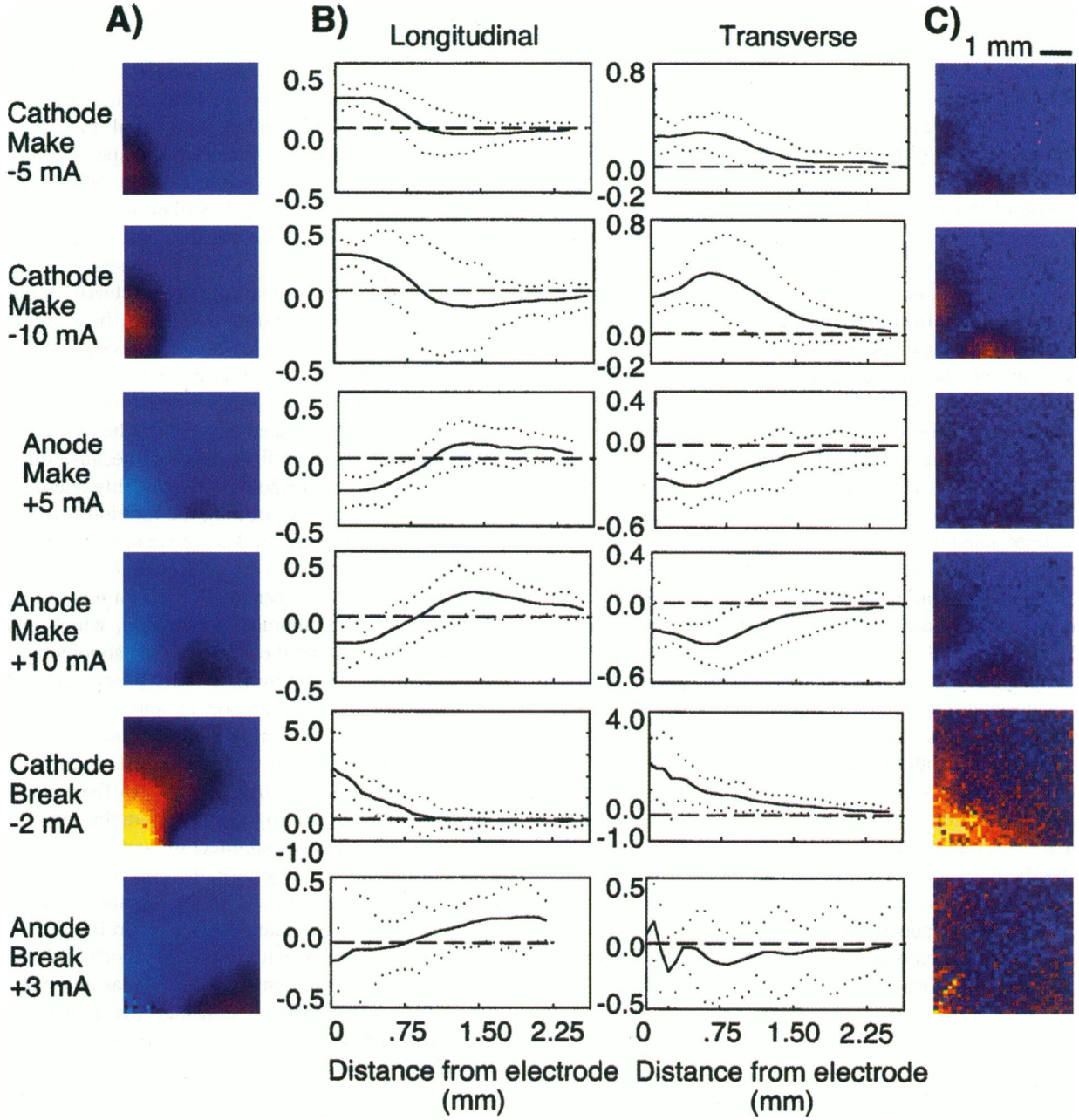

FIGURE 6 (*A*) Folded average images for cathodal make (−5 and −10 mA), anodal make (+5 and +10 mA), cathodal break (−2 mA) and anodal break (+3 mA) stimulation. The average images were divided into quadrants with the origin at the center of intensity and averaged. Before averaging, each quadrant was flipped so that the electrode is in the bottom left corner. Outward longitudinal propagation is toward the right, and outward transverse propagation is upward. (*B*) The normalized fractional change in fluorescence as a function of distance from the electrode in the longitudinal and transverse directions obtained from the folded images in (*A*). The dotted lines are the standard deviation; the dashed straight line is the zero line, with depolarization above it and hyperpolarization below. (*C*) Standard deviation images for column (*A*).

the most important features of the virtual electrode patterns in Fig. 6 occur within 1 mm of the stimulating electrode points out the need for high-resolution images or electrode arrays to study these phenomena.

Our images of the complementary transmembrane potential distributions elicited by positive and negative current injection into refractory tissue, as well as the patterns associated with anodal and cathodal make and break stimulation, directly confirm the predictions of two- and three-dimensional unequal-anisotropy bidomain models for cardiac tissue (Sepulveda et al., 1989; Roth and Wikswo, 1994; Wikswo, 1994a; Roth, 1995a). Model studies show that these complex patterns of virtual cathodes and anodes cannot exist if the anisotropies of the electrical resistivity are the same for both the intracellular and extracellular spaces. Hyperpolarization consistent with virtual anodes

during the injection of current into refractory, depolarized tissue has been observed in the frog heart and rabbit heart (Knisley et al., 1994; Neunlist and Tung, 1994a,b, 1995; Knisley and Davis, 1994; Knisley, 1995). All of these experimental observations provide convincing evidence that there are significant differences between the anisotropies of the two spaces.

Because of the excellent spatial and temporal resolution of our imaging system, we were able to visualize not only the detailed shape of the virtual electrodes, but also the complex configuration of the action potential wave front as it propagates away from the virtual electrodes. The results we report in this paper demonstrate for the first time that cathodal and anodal break stimulation in cardiac tissue is the result of virtual cathodes created adjacent to the stimulating electrodes. These results, combined with our earlier measurements of the virtual cathode in the in vivo canine heart (Wikswo et al., 1991) and the quatrefoil magnetic field produced by canine cardiac slices (Staton et al., 1993), demonstrate unequivocally that the bidomain model with unequal anisotropy ratios provides an excellent representation of the electrical behavior of cardiac muscle at the millimeter spatial scale. Other predictions of this model that require experimental confirmation are block of propagating activation by the virtual anodes, virtual electrodes produced by fiber curvature, alteration of virtual electrode shape by ion-channel blockers, and a stable, quatrefoil reentry pattern (Wikswo, 1994b; Roth, in press). All of these effects are the result of differences in the anisotropies of the electrical conductivities of the intracellular and extracellular spaces. Given the excellent qualititative agreement of these data with the theoretical predictions, the next logical step would be to adjust key parameters of the bidomain models to provide the best quantitative fit to the observed data, and hence to determine physiologically correct electrical parameters for the rabbit heart.

Three-dimensional effects

Whereas the early unequal-anisotropy models were two-dimensional and assumed a passive, linear membrane (Sepulveda and Wikswo, 1987; Sepulveda et al., 1989), more recent calculations have treated the heart as three-dimensional tissue either with an active membrane and a uniform fiber direction (Roth and Wikswo, 1994; Roth, 1995a), or with a passive membrane and a rotating fiber direction (Sepulveda et al., 1991). The three-dimensional models show that the epicardial potentials and the virtual cathodes and anodes produced by point epicardial stimulation are qualitatively the same as those predicted by two-dimensional models.

Understanding of break excitation requires a model with an active membrane, and all of these nonlinear model calculations were three-dimensional representations of cardiac tissue. However, these models assumed a uniform fiber direction throughout. Because of the computational difficulty, we have yet to create nonlinear models with a depth-dependent fiber axis. A linear finite element model was used to compare three-dimensional models with and without fiber rotation (Sepulveda et al., 1991). This study demonstrated that the shapes of the epicardial transmembrane isopotential contours, and hence the shape of the virtual cathodes and anodes as viewed on the epicardium, are essentially the same, regardless of fiber orientation, with the exception that the epicardial patterns exhibit a slight twist. In our earlier experiments on the in situ canine heart (Wikswo et al., 1991), we saw this twist clearly in only one of six dogs studied, suggesting that it may be a small effect compared to other possible factors affecting the virtual cathode shape. Deeper in the tissue, the model showed that the portions of the virtual anodes furthest from the electrode had a slight rotation-induced distortion. The axis of the dog bone rotated to track the fiber axis, but because the virtual cathode for realistic thresholds extended only one-quarter of the thickness of the myocardium, the rotation was less than 25°. Because the virtual anodes are weaker than the virtual cathode, they did not extend as deep into the tissue. The most notable effect of fiber rotation was a helicity in the 0 mV (resting) transmembrane isopotential, which extended deep into the tissue, but the shape of this isopotential would have little effect on the initiation and propagation of activation from the virtual cathode or anode. In the present study, we find that the virtual cathode and anode are not perfectly symmetrical, but we are unable to ascertain as yet how much these asymmetries are due to fiber rotation as compared to local heterogeneities in rabbit myocardium arising from fiber bundle architecture, connective tissue, or cardiac vasculature. In any case, the observed shapes of the virtual cathodes and anodes and the locations where propagating activation is initiated that we report in this paper are in excellent agreement with all of our model calculations, both two- and three-dimensional and linear and nonlinear.

It is also worthwhile to consider the possibility that activation will reach the Purkinje network on the endocardial surface of the rabbit heart. One approach to avoiding this would be to freeze the endocardial surface and thereby ensure that only a thin layer of epicardial tissue was active (Knisley et al., 1994). We chose not to use this preparation because the model studies have yet to address the effects on two-dimensional propagation over a substrate of passive yet highly anisotropic tissue. Because the freezing of the tissue will undoubtedly rupture cell membranes, the electrical anisotropy of the intracellular and extracellular spaces would be altered in an undetermined manner. Thus there exists the possibility that in our preparation, activation could enter the Purkinje system, whose excitability and propagation velocity are appreciably greater that those of working muscle in the epicardium and mid-myocardium. Under such conditions, one might expect that epicardial activation would result from wave fronts breaking through the subendocardium rather than from direct make or break excitation of the epicardium. There are several reasons why we do not believe that these effects occur in the data we

have presented. Because we are using point epicardial stimuli with a large counter electrode on the opposite side of the heart, the stimuli are not strong enough to directly stimulate the endocardium or the Purkinje system. This is consistent with model calculations that show activation beginning to propagate from the edge of the virtual cathode or anode, which are relatively close to the stimulating electrode. Although activation originating on the surface will propagate into the myocardium and eventually reach the epicardium, it will do so with the lower transverse propagation velocity. If the Purkinje system is activated in this manner, the resulting propagation will return to the surface again with the slower, transverse velocity. In our studies, we are examining data from cathodal and anodal make stimulation for only the first 8 ms after the stimulus and within 3–4 mm of the stimulus electrode. By 4 ms, the spread of epicardial activation is dominated by the rapid, longitudinal activation. During the 8 ms spanned by our images, there is inadequate time for propagating activation to reach the endocardium and return to a region of excitable epicardium. Obviously, were we to study activation further from the stimulus site and at longer times after stimulus, we might expect that the activation patterns could shift from small shells of activation driven by epicardial events into larger, transmural wave fronts driven by Purkinje activation. For break excitation, the bulk myocardium is refractory, and excitation occurs in the immediate vicinity of the virtual anodes, where the tissue is hyperpolarized by the stimulus. Although the same endocardial effects might occur, they will do so even later and further from the stimulus electrode.

Tissue nonlinearity

We have yet to ascertain the extent to which the voltage and time dependence of the membrane conductance affects the size and shape of the virtual electrodes. The theory (Roth, 1995a) predicts that changes in membrane conductance play a role in anodal break stimulation. We have yet to acquire sufficient data at multiple stimulus strengths to determine whether virtual electrode size has the logarithmic dependence upon stimulus current that is predicted by linear models and was observed in the previous electrode/back-extrapolation measurements (Wikswo et al., 1991), or whether membrane nonlinearities play a role.

Alternative models

The propagating, three-dimensional waves of electrical activation that are responsible for either the normal, rhythmic cardiac contractions or more complex patterns, such as those of fibrillation, are made possible by the coupling of adjacent myocardial cells by gap junctions within the intercalated disks to form a functional syncytium. The earliest mathematical models of cardiac tissue assumed that the tissue could be modeled by a homogeneous, isotropic conductor, i.e., a monodomain, upon which would be superimposed active current sources, corresponding to the cardiac cells that were in the process of being depolarized. However, the cylindrical shape of cardiac cells, their branching, and the distribution of gap junctions produce a directional dependence, i.e., anisotropy, of key parameters, such as a 2:1 ratio of conduction velocity longitudinal versus transverse to the fibers and a similar ratio of the electrical conductivities of the bulk muscle (Rush et al., 1963). Thus, later models required the addition of either anisotropy or non-uniform, fiber-oriented wave fronts to explain recordings of extracellular potentials in advance of small, expanding action potential wave fronts (Corbin and Scher, 1977), but such models did not provide a coupling between macroscopic potential distributions and membrane physiology.

A proposed model predicted that the electrical discontinuities formed by the high resistance across the intercalated disks between cardiac cells would lead to the depolarization of one end of each cell and the hyperpolarization of the other during current injection (Plonsey and Barr, 1986). Although this effect has been described in single isolated cardiac myocytes in the presence of defibrillation-strength electric fields (Knisley et al., 1993), the predicted spatial variation of the transmembrane potential associated with the resistive discontinuities has not yet been found experimentally within a single cell that is coupled to neighboring cells in situ.

Only the bidomain model with unequal anisotropy has been able to explain the observed quatrefoil magnetic field, the dog-bone-shaped virtual cathode, the anodal regions adjacent to cathodal stimuli, and the ability of cathodal break and anodal make and break stimuli to excite the heart. Despite these successes, it is likely that the homogeneous, unequal-anisotropy bidomain model will eventually be further enhanced by the incorporation of small-scale discontinuities, such as those between cells or between fiber bundles.

Limitations of the technique

Camera system

A variety of approaches have been developed to use voltage-sensitive dyes to measure the spatial and temporal dependence of action potentials propagating through cardiac tissue. Photodiode arrays and laser scanning systems provide good time resolution at a limited number of points (Dillon and Morad, 1981; Salama et al., 1987; Hill and Courtney, 1987). Fiber optic systems provide excellent signal-to-noise ratios at one or two points (Bowmaster et al., 1991; Neunlist et al., 1992) and can be used to map out virtual electrodes at a small number of locations (Neunlist and Tung, 1994a,b, 1995). High-speed video techniques provide images with a large number of pixels and can be used to create impressive movies of propagating activation and reentry (Davidenko et al., 1991; Pertsov et al., 1993); however, the effective shutter open time of these video cameras is sufficiently long (typically 16 ms) that the edges

of the activation wave fronts are blurred to the extent that it would be difficult to examine the detailed evolution of the activation wave fronts in the first few milliseconds after stimulation, and the limited dynamic range of these cameras complicates data acquisition and analysis. The approach we have taken represents a compromise that provides high spatial resolution, 0.5-ms exposure times, a 2-ms or shorter frame interval, and a 12-bit dynamic range. In exchange for these capabilities, we are at present limited to using boxcar averaging techniques to create movies that are only several frames long, and we are not able to study asynchronous or nonstationary phenomena such as ectopic beats or reentry. Future enhancements to our camera should extend the capabilities of our imaging system.

As we discussed above, we are utilizing a preparation in which the entire heart is excitable, in contrast to frozen endocardium preparations for which only an epicardial layer is active. In our case, excited tissue beneath the surface can contribute to the fluorescence signals and could lead to a blurring of the wave fronts. Because we are concentrating on the initiation of activation, which will occur first on the epicardial surface, the contributions of deeper tissue at a given distance from the electrode will occur later and hence on any single frame will appear on the inner edges of the propagating wave fronts; the effect will be largest for areas of faster, longitudinal propagation, and may contribute to the observed width of the longitudinal activation in the later frames of Fig. 3, *A* and *D*. More detailed measurements, probably requiring transmural electrodes and shorter frame intervals, will be needed to clarify this effect.

Stimulation electrode

Because the stimulating wire is in the center of the field, and it is supported by a suture that crosses the field, the details of activation within several hundred microns of the center of the stimulus are not readily visible. Because this study was directed toward the identification of the onset of propagating activation at the edges of the virtual cathodes and anodes located a millimeter or more from the electrode, the loss of information under the electrode did not limit the present study.

The use of strong stimuli

The theoretical predictions reviewed above and confirmatory experimental studies (Wikswo et al., 1991) indicate that the sizes of the virtual electrodes are dependent upon the strength of the stimulus. The bidomain model shows that for any stimulus strength, the transmembrane isopotentials are dog-bone-shaped only beyond a millimeter from the electrode. Hence for threshold cathodal make stimuli, the virtual cathode will be small and will not have the dog bone shape, and the virtual anodes will be distant and only weakly hyperpolarized. As the stimulus strength is increased, the isopotential contour that corresponds to the membrane threshold (and hence defines the edge of the virtual cathode) will lie further from the stimulus electrode and the virtual cathode will be larger. For adequately strong stimuli, typically 10 times threshold, the threshold isopotential will be 1 to 2 mm from the electrode and hence will exhibit the dog bone shape. For such strong stimuli, the adjacent virtual anodes will be strongly hyperpolarized and can affect the propagation that originates from the virtual cathode that lies between the virtual anode and the stimulus electrode. Similarly, the effects responsible for anodal make and both cathodal and anodal break stimulation require strong virtual cathodes and anodes, and hence require higher stimulus strengths. As discussed under Materials and Methods, these strong stimuli can lead to tissue damage, particularly with repeated, long anodal or cathodal break stimuli. Damaged tissue immediately adjacent to the stimulus electrode would become passive and would effectively increase the size of the physical electrode. The effects we report occur far beyond any possible region of tissue damage. The possibility of tissue damage could have been reduced by using a larger stimulus electrode, but that would have made the measurements less representative of the model calculations being tested.

The use of diacetylmonoxime

Currently, optical imaging in mammalian hearts requires the use of a contraction-blocking agent, such as diacetylmonoxime, to eliminate motion artifact. As shown by Liu et al. (1993), this can cause a small, reversible, nonselective reduction of several membrane conductances and a concomitant decrease in action potential duration and a slight reduction in conduction velocity. Although this may result in quantitative changes in virtual electrode size and shape, it is unlikely that diacetylmonoxime will have any effect on the overall phenomena we report.

Effects of averaging across experiments

As a result of unavoidable inter-site and inter-animal variation in stimulus threshold and conduction velocity, the averaged images in Figs. 4–6 are broadened over the single-experiment images in Figs. 2 and 3. A camera with a faster frame speed would obviate the need for the boxcar averaging techniques and would reduce the number of stimuli required for a single frame, thereby allowing the same number of stimuli to be used to obtain more frames and hence a cleaner set of averaged images for each experiment, or for more values of I_s for a given tissue region. For the average images, we chose fixed stimulus currents of ± 5 and ± 10 mA for cathodal and anodal make stimulation, -2 mA for cathodal break, and $+3$ mA for anodal make. These values were in the range of 5 to 10 times threshold; were more data available, it would be possible to determine the extent to which the inter-experiment variation was determined by variations in stimulus threshold. Even with the limitations of the present system, the images averaged across experiments are quite consistent and provide a clear

indication of the role of virtual electrodes in the stimulation of cardiac tissue. However, this analysis approach reduces the effects of fiber curvature if there are differences between sites and animals. The fiber axis was represented by a straight line through the entire recording region, whereas the actual fiber axis may have been changing. Similarly, the images were summed about a center corresponding to a single point, and asymmetries in the images may have affected the simple algorithms that determined automatically the center and fiber axis. In the data in Fig. 6, the reflection of the second through fourth quadrants into the first increases the signal-to-noise ratio but also eliminates any asymmetries in the data. Hence these results cannot address the effects of fiber curvature or rotation on virtual electrodes. However, these data represent an average response to the stimulus current and hence could be used with theoretical models to determine average values of particular tissue parameters.

Definition of the edges of the virtual electrodes

In our earlier work we defined the edge of the virtual cathode as the locus of points for which the transmembrane potential reached the threshold value (Wikswo et al., 1991; Sepulveda et al., 1989). Because the threshold is determined by the duration, sign, and timing of the stimulus, this is somewhat simplistic. As shown in Fig. 6 *B*, the virtual electrodes do not have sharp edges, and hence it is difficult, except for the zero crossing between an adjacent virtual cathode and anode, to define precise boundaries from measurements of the transmembrane potential distribution at the end of the stimulus pulse. For those virtual electrodes that are the source of a propagating wave front, the sequential imaging of these wave fronts might be used to determine the locus of points that represents the earliest propagating wave front. Undoubtedly, the early wave fronts may exhibit a transient alteration in conduction velocity due to electrotonic effects lingering after the stimulus, and from curvature-dependent velocity arising from the complex shape of the virtual electrodes. The velocity will stabilize only after the wave front enlarges beyond both the range of influence of the opposite-signed virtual electrode and the region where the curvature dependence and the electrotonic effects are significant. Future studies will address the initiation of action potential propagation from the virtual electrodes.

Implications

The flow of current in multidimensional, anisotropic cables can produce effects that are not predicted by one-dimensional models. The anisotropy in the electrical conductivity implies that current flow need not be parallel to the local electric field (i.e., the potential gradient); the differences in anisotropy between the intracellular and extracellular spaces further imply that the division of current between the intracellular and extracellular spaces does not obey a simple length constant, as occurs in one-dimensional cables, but is determined by the overall potential distribution in each space. The full implications of these anisotropic bidomain effects are not yet known. It is clear from this work that the current injection into the extracellular space of tissue with unequal anisotropies simultaneously produces distinct depolarized and hyperpolarized regions of transmembrane potential that are the mechanism by which anodal make and anodal break excitation occur. These adjacent regions of hyperpolarization and depolarization may also produce a directionally dependent modification of the refractory period of cardiac tissue that could provide a mechanism for the reentrant arrhythmias that are produced by strong and/or repetitive high-frequency pacing stimuli in the canine and human heart. The defibrillation of cardiac tissue involves the injection of strong currents, and there are undoubtedly large regions of the heart that are either virtual cathodes or virtual anodes. More detailed mathematical models and experimental measurements will be required to further understand the role of unequal anisotropies in human cardiac physiology and pathology.

We are grateful to Dan M. Roden and Bradley J. Roth for their encouragement and numerous suggestions, to Leonora Wikswo for her comments on the manuscript, and to Stephen B. Knisley for enjoyable discussions and for demonstrating to us the rabbit heart staining technique. We appreciate a number of helpful comments by the reviewers.

This work has been supported by National Institutes of Health grant P01HL46681.

REFERENCES

Barach, J. P., and J. P. Wikswo, Jr. 1992. A numerical reconstruction of the effects of late stimulation on a cardiac ventricular action potential. *Comp. Biomed. Res.* 25:212–217.

Beeler, G. W., and H. Reuter. 1977. Reconstruction of the action potential of ventricular myocardial fibers. *J. Physiol.* 268:177–210.

Bowmaster, T. A., C. C. Davis, and V. Krauthamer. 1991. Excitation and detection of action potential-induced fluorescence changes through a single monomode optical fiber. *Biochim. Biophys. Acta.* 1091:9–14.

Clerc, L. 1976. Directional differences of impulse spread in trabecular muscle from mammalian heart. *J. Physiol.* 255:335–346.

Cohen, L. B., and S. Lesher. 1986. Optical monitoring of membrane potential: methods of multisite optical measurement. *In* Optical Methods in Cell Physiology. P. De Weer and B. M. Salzberg, editors. Wiley-Interscience, New York. 71–99.

Corbin, L. V., II, and A. M. Scher. 1977. The canine heart as an electrocardiographic generator: dependence on cardiac cell orientation. *Circ. Res.* 41:58–67.

Davidenko, J. M., A. M. Pertsov, R. Salomonsz, W. T. Baxter, and J. Jalife. 1991. Stationary and drifting spiral waves of excitation in isolated cardiac muscle. *Nature.* 355:349–351.

Dekker, E. 1970. Direct current make and break thresholds for pacemaker electrodes on the canine ventricle. *Circ. Res.* 27:811–823.

Dillon, S., and M. Morad. 1981. A new laser scanning system for measuring action potential propagation in the heart. *Science.* 214:453–455.

Ebihara, L., and E. A. Johnson. 1980. Fast sodium current in cardiac muscle. *Biophys. J.* 32:779–790.

Eisenberg, R. S., V. Barcilon, and R. T. Mathias. 1979. Electrical properties of spherical syncitia. *Biophys. J.* 25:151–180.

Geselowitz, D. B., and W. T. Miller. 1983. A bidomain model for anisotropic cardiac muscle. *J. Biomed. Eng.* 11:191–206.

Henriquez, C. S., and R. Plonsey. 1990a. Simulation of propagation along a cylindrical bundle of cardiac tissue. I. Mathematical formulation. *IEEE Trans. Biomed. Eng.* 37:850–860.

Henriquez, C. S., and R. Plonsey. 1990b. Simulation of propagation along a cylindrical bundle of cardiac tissue. II. Results of simulation. *IEEE Trans. Biomed. Eng.* 37:861–875.

Hill, B. C., and K. R. Courtney. 1987. Design of a multi-point laser scanned optical monitor of cardiac action potential propagation: application to microreentry in guinea pig atrium. *Ann. Biomed. Eng.* 15: 567–577.

Knisley, S. B. 1995. Transmembrane voltage changes during unipolar stimulation of rabbit ventricle. *Circ. Res.* 77: In press.

Knisley, S. B., T. F. Blitchington, B. C. Hill, A. O. Grant, W. M. Smith, T. C. Pilkington, and R. E. Ideker. 1993. Optical measurements of transmembrane potential changes during electric field stimulation of ventricular cells. *Circ. Res.* 72:255–271.

Knisley, S. B., and C. T. Davis. 1994. Membrane polarization during point stimulation in perfused rabbit hearts. *Circulation.* 90:I-176.

Knisley, S. B., B. C. Hill, and R. E. Ideker. 1994. Virtual electrode effects in myocardial fibers. *Biophys. J.* 66:719–728.

Lim, J. S. 1990. Two-Dimensional Signal and Image Processing. Prentice Hall, London. 536–540.

Liu, Y., C. Cabo, R. Salomonsz, M. Delmar, J. Davidenko, and J. Jalife. 1993. Effects of diacetyl monoxime on the electrical properties of sheep and guinea pig ventricular muscle. *Cardiovasc. Res.* 27:1991–1997.

Muler, A. L., and V. S. Markin. 1977a. Electrical properties of anisotropic nerve-muscle syncytia. I. Distribution of the electrotonic potential. *Biofizika.* 22:307–312.

Muler, A. L., and V. S. Markin. 1977b. Electrical properties of anisotropic nerve-muscle syncytia. II. Spread of flat front of excitation. *Biofizika.* 22:518–522.

Muler, A. L., and V. S. Markin. 1977c. Electrical properties of anisotropic nerve-muscle syncytia. III. Steady form of the excitation front. *Biofizika.* 22:671–675.

Neunlist, M., and L. Tung. 1994a. Optical recordings of ventricular excitability of frog heart by an extracellular stimulating point electrode. *Pacing Clin. Electrophysiol.* 17:1641–1654.

Neunlist, M., and L. Tung. 1994b. Optical recordings of cardiac transmembrane potential around an extracellular electrode in electrically anisotropic bullfrog atrium. *In* Proceedings of the 16th Annual International Conference of the IEEE Engineering in Medicine and Biology Society. IEEE, Piscataway. 43–44.

Neunlist, M., and L. Tung. 1995. Spatial distribution of cardiac transmembrane potentials around an extracellular electrode. Dependence on fiber orientation. *Biophys. J.* 68:2310–2322.

Neunlist, M., S.-Z. Zou, and L. Tung. 1992. Design and use of an "optrode" for optical recordings of cardiac action potentials. *Pflügers Arch.* 420: 611–617.

Pertsov, A. M., J. M. Davidenko, R. Salomonsz, W. T. Baxter, and J. Jalife. 1993. Spiral waves of excitation underlie reentrant activity in isolated cardiac muscle. *Circ. Res.* 72:631–650.

Plonsey, R., and R. C. Barr. 1984. Current flow patterns in two-dimensional anisotropic bisyncytia with normal and extreme conductivities. *Biophys. J.* 45:557–571.

Plonsey, R., and R. C. Barr. 1986. Effect of microscopic and macroscopic discontinuities on the response of cardiac tissue to defibrillation (stimulating) currents. *Med. Biol. Eng. Comp.* 24:130–136.

Roth, B. J. 1995a. A mathematical mode of make, and break electrical stimulation of cardiac tissue by a unipolar anode or cathode. *IEEE Trans. Biomed. Eng.* In press.

Roth, B. J. The bidomain model of cardiac tissue: predictions and experimental verification. *In* Neural Engineering. Y. Kim and N. Thakor, editors. Springer-Verlag, New York. In press.

Roth, B. J., and J. P. Wikswo, Jr. 1986. A bidomain model for the extracellular potential and magnetic field of cardiac tissue. *IEEE Trans. Biomed. Eng.* 33:467–469.

Roth, B. J., and J. P. Wikswo, Jr. 1994. Electrical stimulation of cardiac tissue: a bidomain model with active membrane properties. *IEEE Trans. Biomed. Eng.* 41:232–240.

Rush, S., J. A. Abildskov, and R. Mcfee. 1963. Resistivity of body tissues at low frequencies. *Circ. Res.* 12:40–50.

Salama, G., R. Lombardi, and J. Elson. 1987. Optical maps of action potential propagation and NADH fluorescence in intact working hearts. *Am. J. Physiol.* 252H:384–394.

Sepulveda, N. G., J. P. Barach, and J. P. Wikswo, Jr. 1991. A three dimensional finite element bidomain model for cardiac tissue. *In* Proceedings of the Annual International Conference of the IEEE Engineering in Medicine and Biology Society, New Frontiers of Biomedical Engineering—Innovations from Nuclear to Space Technology, Vol. 13, Part II. J. H. Nagel and W. M. Smith, editors. IEEE, Piscataway. 512–514.

Sepulveda, N. G., B. J. Roth, and J. P. Wikswo, Jr. 1989. Current injection into a two-dimensional anisotropic bidomain. *Biophys. J.* 55:987–999.

Sepulveda, N. G., and J. P. Wikswo, Jr. 1987. Electric and magnetic fields from two-dimensional anisotropic bisyncytia. *Biophys. J.* 51:557–568.

Staton, D. J., R. N. Friedman, and J. P. Wikswo, Jr. 1993. High resolution SQUID imaging of octupolar currents in anisotropic cardiac tissue. *IEEE Trans. Appl. Supercond.* 3:1934–1936.

Trayanova, N. A. 1994. A bidomain model for ring stimulation of a cardiac strand. *IEEE Trans. Biomed. Eng.* 41:393–397.

Tung, L. 1978. A bidomain model for describing ischemic myocardial D. C. potentials. Ph.D. dissertation. Massachusetts Institute of Technology, Cambridge.

Wikswo, J. P., Jr. 1994a. The complexities of cardiac cables: virtual electrode effects. *Biophys. J.* 66:551–553.

Wikswo, J. P., Jr. 1994b. Tissue anisotropy, the cardiac bidomain and the virtual cathode effect. *In* Cardiac Electrophysiology: From Cell to Bedside, 2nd ed. D. P. Zipes and J. Jalife, editors. W. B. Saunders, Orlando. 348–361.

Wikswo, J. P., Jr., W. Altemeier, J. R. Balser, H. A. Kopelman, T. Wisialowski, and D. M. Roden. 1991. Virtual cathode effects during stimulation of cardiac muscle: two-dimensional in vivo measurements. *Circ. Res.* 68:513–530.